Pergamon

Int. J. Heat Mass Transfer. Vol. 38, No. 10, pp. 1841–1853, 1995

0017-9310/95 $9.50+0.00

0017-9310(94)00305-X

Numerical computation of fluid flow of floating-zone crystal growth of molybdenum

J.-C. CHEN and C.-F. CHU

Department of Mechanical Engineering, National Central University, Chung-Li, Taiwan 32054, R.O.C.

(*Received* 22 *July* 1994 *and in final form* 5 *September* 1994)

Abstract—The heat transfer and fluid flow in the floating-zone crystal-growth process for molybdenum (Mo) materials is studied numerically. The input power induced by the heat source is assumed to be a Gaussian distribution. The steady, axisymmetric flow and temperature fields are solved using a finite difference method, employing a boundary-fitted curvilinear coordinate system. The shape of the molten zone and the temperature and velocity fields in the melt are coupled and are strongly dependent on the magnitude of the input power. A four-cell flow structure in the melt is obtained. The effect of thermocapillary convection is much more significant than that of buoyancy-driven convection. The results show that the steady, axisymmetric flow may not exist when the strength of the flow reaches a certain magnitude, which varies insignificantly with the change of the heating region and the rod diameter. The present results are in good agreement with experimental results.

1. INTRODUCTION

In a floating-zone crystal-growth process, two types of natural convection may occur in the molten zone due to the non-uniform temperature distribution: buoyancy-driven flow induced by the density gradients inside the melt, and thermocapillary flow generated by the surface-tension gradients along the free surface of the melt. Barthel *et al.* [1] have found that the radial impurity distribution in Mo single crystals grown by the electron beam floating-zone method is governed by the flow structure in the molten zone. The convective transport present in the melt can significantly affect the shape and stability of the zone, which determine the structure and quality of the resultant crystals. Convection instability was thought to be responsible for the presence of striations in the crystals. Striations in single silicon (Si) and molybdenum (Mo) crystals were believed to be due to oscillatory thermocapillary convection [2, 3]. Kitamura *et al.* [4] found that the shape of the solid–liquid interface during the floating-zone growth affects the properties of the resultant crystal such as dislocation density, presence of inclusions and cracks. They believe that, to grow a high quality single crystal, the interface must be flat or convex towards the melt.

To study the convection phenomena, the floating zone has typically been simplified by vertical liquid bridges held between two concentric, cylindrical heated rods. In this model, the zone length and the heating condition can be selected independently and the effect of the shape of the solid–melt interface is excluded. Chang and Wilcox [5], Jurisch *et al.* [6], Kobayashi [7], Fu and Ostrach [8] and Chen *et al.* [9] performed numerical computations to investigate the flow structure of the steady, axisymmetric thermocapillary flow in liquid bridges. Experiments on thermocapillary convection in liquid bridges performed by Schwabe *et al.* [10], Chun [11], Preisser *et al.* [12], Kamotani *et al.* [13] and Velten [14] show that a steady flow may change into an oscillatory flow when a dimensionless parameter, the Marangoni number, which governs the strength of the thermocapillary convection, exceeds a critical value and other parameters are kept fixed.

In the real floating-zone crystal process, the temperature fields, the flow fields in the molten zone, and the zone shape are coupled and are strongly dependent on the magnitude of input power. Therefore, the aspect ratio cannot be varied arbitrarily. This is the major difference between real floating-zone systems and liquid-bridge models. To better understand the transport phenomena in the floating-zone growth, a numerical simulation should be able to take into account those effects. Lan and Kuo [15–17] assume an ambient temperature distribution to investigate the interaction between the fluid flow and the solid–melt interface in the float-zone crystal-growth process. In real systems, the ambient temperature distribution is unknown *a priori*, but the power supplied by the external source is easily obtained. Chen *et al.* [18] investigated the interaction between the thermocapillary convection and the zone shape for different strengths of the uniformly distributed input power. Their results show that the shape of the molten zone is significantly affected by the Prandtl number. For small Prandtl number fluids, when the input power increases, the solid–melt interface varies from convex towards the melt, through flat to concave, and the thermocapillary-flow instability in the melt may appear

NOMENCLATURE

Bi_c	convection Biot number
Bi_r	radiation Biot number
Bo_{dyn}	dynamic Bond number
g	gravitational acceleration
Gr	Grashof number
h	surface heat transfer coefficient
$i_1(r)$	dimensionless shape function of the upper solid–melt interface
$i_2(r)$	dimensionless shape function of the lower solid–melt interface
k	thermal conductivity
L	dimensionless length of the material rod
L_c	zone height at the centerline of the rod
L_s	zone height at the surface of the rod
Ma	Marangoni number
P	dimensionless power
Pr	Prandtl number
q	power distribution
q_0	power density
Q	dimensionless power distribution
Q_0	dimensionless power density
r	dimensionless radius coordinate
Re	Reynolds number
Rt	T_∞/T_m
r_0	radius of the material rod
s	standard deviation of the Gaussian distribution
St	Stefan number
T	temperature
T_m	melting temperature
T_∞	ambient temperature
u	dimensionless radial velocity
v	dimensionless axial velocity
V_p	dimensionless pulling velocity
z	dimensionless axial coordinate.

Greek symbols

α	thermal diffusivity
β	thermal expansion coefficient
ΔL	latent heat
γ	surface-tension temperature coefficient
ε	emissivity
Λ	thermal conductivity ratio
λ	density ratio
Θ	dimensionless temperature
Θ_{max}	maximum temperature
μ	dynamic viscosity
ν	kinematic viscosity
ρ	density
σ	Stefan–Boltzmann constant
ψ	stream function
Ψ	$\psi\, Pr\, Re$
ω	vorticity.

Subscripts

l	liquid phase
n	normal derivative on the solid–melt interface
r, z	derivatives with respect to r, z
s	solid phase.

before the capillary instability (originating from the gas–melt interface) sets in. For higher Prandtl number fluids, the solid–liquid interface is always convex towards the melt and the appearance of capillary instability is more likely than thermocapillary-flow instability.

In molten metals and semiconductors, which are low Prandtl number fluids, the momentum transfer is vigorous. The order of the Reynolds number is higher than O(10^6). Therefore, the flow structure in molten metals and semiconductors is very complicated. Experimental observations of transport phenomena in metal and semiconductor melts during the floating-zone process are very difficult since the temperature in the melt exceeds 1000 K and the melt becomes incandescent. On the other hand, the numerical simulations are still limited in scope. Lan and Kuo [16] considered the effect of the buoyancy-driven flow on the thermocapillary convection for Si materials. Chen *et al.* [18] considered the small Reynolds number case. In the present paper, the heat transfer and fluid flow in the floating-zone process is investigated numerically. The distribution of the input power induced by the heat source is assumed to be Gaussian. The numerical scheme is a modified version of that used by Chen *et al.* [18] with the inclusion of the effect of buoyancy-driven convection. Computations have been performed for a small Prandtl number material: molybdenum (Mo). The effect of power distribution and diameter of the material rod are considered. The present results are compared with experimental results [3].

2. GOVERNING EQUATION AND BOUNDARY CONDITIONS

A schematic diagram of the floating-zone crystal-growth system is illustrated in Fig. 1. The input power distribution due to the heat source is assumed to be Gaussian and is stated as follows:

$$q(z) = \frac{q_0}{s\sqrt{2\pi}} e^{-1/2(z/sr_0)^2} \tag{1}$$

where q_0 is the density of the input power and the parameter s is the standard deviation of the distribution. We set that about 99% of the input power lies in the range of $-2.58s < z/r_0 < 2.58s$. The melt from

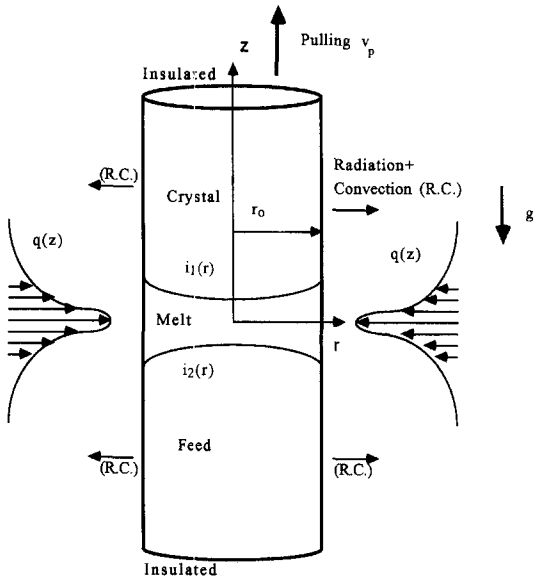

Fig. 1. Schematic diagram of the floating-zone system.

the rod contains an incompressible, Newtonian liquid. Based on the results of Lan and Kuo [16], we can expect that the flow and temperature fields will be modified by the large surface deformation of the gas–melt interface. For the present case, the surface deformation is small because the mean surface tension of Mo is very large and the rod diameter considered is small. To simplify the analysis, the gas–melt interface is assumed to be flat. The surface tension is considered as a linear decreasing function of temperature, and the Boussinesq approximation has been assumed to be valid for density variation. The flow motion inside the melt is assumed to be steady, axisymmetric, and laminar. The cylindrical coordinates and the input power are considered to be fixed.

The variables of length, velocity and pressure have been made dimensionless using the scales r_0, $(\gamma T_m)/\mu$ and $(\gamma T_m)/r_0$, respectively; r_0 is the radius of the material rod, μ is the viscosity of the melt, γ is the negative rate of change of surface tension with temperature and T_m is the melting temperature. The dimensionless temperature is defined by $\Theta = (T - T_m)/T_m$. The dimensionless equations for the stream function–vorticity–temperature form are in the following form

$$Re\left(-\frac{\omega}{r^2}\psi_z + \frac{1}{r}\psi_z\omega_r - \frac{1}{r}\psi_r\omega_z\right) = \omega_{rr} + \frac{1}{r}\omega_r + \omega_{zz} - \frac{1}{r^2}\omega - \frac{Gr}{Re}\Theta_r \quad (2)$$

$$\psi_{rr} - \frac{1}{r}\psi_r + \psi_{zz} = r\omega \quad (3)$$

$$Pr \cdot Re\left(\frac{1}{r}\psi_z\Theta_r - \frac{1}{r}\psi_r\Theta_z\right) = \Theta_{rr} + \frac{1}{r}\Theta_r + \Theta_{zz} \quad (4)$$

where $\psi = -V_p r^2/2$ in the solid region. The stream function ψ and the vorticity ω are given by

$$u = \frac{1}{r}\psi_z \quad v = -\frac{1}{r}\psi_r \quad (5)$$

and

$$\omega = u_z - v_r. \quad (6)$$

The subscripts r and z denote the partial derivatives $\partial/\partial r$ and $\partial/\partial z$, respectively. The Prandtl, Reynolds and Grashof numbers are defined by

$$Pr = \nu/\alpha$$

$$Re = \gamma T_m r_0/\mu\nu$$

$$Gr = \rho l^2 g\beta T_m r_0^3/\mu^2$$

where α is the thermal diffusivity, ν is the kinematic viscosity, β is the thermal expansion coefficient and g is the gravitational acceleration.

The appropriate boundary conditions are as follows:

(i) symmetry at the center line

$$\Theta_r = \psi = \omega = 0 \quad \text{at } r = 0 \quad (7)$$

(ii) energy balance at the solid–gas interface of the material rod

$$-\Theta_r = Bi_r[(\Theta+1)^4 - Rt^4] + Bi_c(\Theta + 1 - Rt) - Q(z) \quad \text{at } r = 1 \quad (8)$$

(iii) energy balance at the melt–gas interface of the molten zone

$$-\Lambda\Theta_r = Bi_r[(\Theta+1)^4 - Rt^4] + Bi_c(\Theta + 1 - Rt) - Q(z) \quad \text{at } r = 1 \quad (9)$$

(iv) no normal velocity and shear stress balance at the melt–gas interface in the molten zone,

$$\psi = -\tfrac{1}{2}\lambda V_p \quad (10)$$

$$\omega = \Theta_z \quad \text{at } r = 1 \quad (11)$$

(v) temperature equal to the melting point at the solid–melt interface

$$\Theta = 0 \quad \text{at } z = i_1(r) \text{ and } i_2(r); \quad (12)$$

(vi) energy balance at the solid–melt interface

$$(\Theta_n)_s - \Lambda(\Theta_n)_l = -\Lambda\, St\, Pr\, Re\, V_p(e_z n) \quad \text{at } z = i_1(r) \text{ and } i_2(r) \quad (13)$$

(vii) no slip and constant upward velocity at the solid–melt interface,

$$\psi = -\lambda V_p r^2/2 \quad (14)$$

$$\psi_{rr} - \frac{1}{r}\psi_r + \psi_{zz} = r\omega \quad \text{at } z = i_1(r) \text{ and } i_2(r) \quad (15)$$

(viii) no heat transfer far from the molten region

$$\Theta_z = 0 \quad \text{at } z = L/2 \text{ and } -L/2 \quad (16)$$

where L is the dimensionless length of the rod and V_p

is the dimensionless pulling speed. The function $Q(z)$ is given by

$$Q(z) = \frac{Q_0}{s\sqrt{2\pi}} e^{-1/2(z/s)^2}. \quad (17)$$

The subscript n denotes the partial derivative of normal direction on the solid–melt interface while the subscripts s and l denote the solid and liquid phases, respectively. The boundary conditions contain the following dimensionless parameters

$Rt = T_\infty/T_m$	dimensionless ambient temperature
$St = \Delta L/c_p T_m$	Stefan number
$\Lambda = k_l/k_s$	thermal conductivity ratio
$\lambda = \rho_s/\rho_l$	density ratio
$Q_0 = q_0 r_0/(k_s T_m)$	dimensionless power density
$Bi_r = \varepsilon\sigma T_m^3 r_0/k_s$	Biot number of radiation
$Bi_c = hr_0/k_s$	Biot number of convection

where T_∞ is the ambient temperature, ΔL is the latent heat, c_p is the specific heat, k_s is the thermal conductivity of the solid region, k_l is the thermal conductivity of the molten zone, ε is the emissivity, σ is the Stefan–Boltzmann constant and h is the surface heat transfer coefficient. The dimensionless power is defined by $P = 2\pi r_0 q_0/k_s T_m = 2\pi Q_0$.

3. SOLUTION PROCEDURE

The shape of solid–melt interface is unknown *a priori* but must be determined as part of the overall solution. By assigning a specific shape to the solid–melt interface and temporarily discarding the Stefan condition (13), a complete solution of the velocity and temperature fields can be determined from the governing equations (2)–(4) and boundary conditions (7)–(16). The Stefan condition then provides a means to examine whether or not the solid–melt interface shape is the required solution, and a basis for computing an improved estimate of that shape when the condition is not satisfied.

The numerical scheme, which is a modified version of that employed previously by Chen *et al.* [18], has been used to solve a system (2)–(4) with conditions (7)–(16). Central-difference formulas with second-order accuracy are used for all spatial derivatives. A more complete discussion of the code appears in ref. [18] and will not be repeated here.

Briefly, the solution procedure involves the following steps:

(1) An initial shape of the solid–melt interface, which is determined by solving the pure conduction equation, is selected.

(2) The liquid and solid regions are transferred to computational domains separately using a boundary-fitted curvilinear coordinate system (Thompson *et al.* [19]) that has coordinate lines coincident with the current boundaries. Grid stretching, which provides good resolution near the free surface and the solid–melt interface, is achieved by employing the grid control method developed by Middlecoff and Thomas [20].

(3) Initial guesses for Θ, ω and ψ over the entire computational domain are then chosen.

(4) The differential equations for ω, ψ and Θ are solved iteratively using the line-successive over-relaxation (LSOR) method. The iteration process is termed to converge when the relative error of two successive iterations is less than 10^{-5}.

(5) The Stefan condition (11) is checked, and if it is not satisfied, the solid–melt interface is modified to reduce the error. The search procedure for the new shape of the solid–melt interface is described in detail in ref. [18].

(6) Return to step (2) and repeat iteratively until all equation and boundary conditions are satisfied.

4. RESULTS AND DISCUSSION

The numerical computations described above were done on the Vax 9320 computer at the National Central University and the IBM ES9000 computer at the National Center for High-Performance Computing using double-precision arithmetic. Calculations were performed for the case in which the dimensionless length of the rod is $L = 20$. The physical properties of Mo selected by the present study are listed in Table 1. According to the Table 1, the Prandtl number Pr, the thermal conductivity ratio Λ, and the density ratio λ for Mo material are 0.025, 1.0 and 1.0, respectively. The parameter Rt is chosen to be 0.104. To compare with the experimental results of Jurisch and Löser [3], the radius of the material rod is selected as $r_0 = 1.0$, 1.3, 2.0 and 3 mm. The corresponding dimensionless parameters are listed in Table 2. The dynamic Bond number, which is usually used to represent the relative importance between the buoyancy-driven flow and the thermocapillary flow, is defined as $Bo_{dyn} = Gr/Re$. For the rod diameter considered, the thermocapillary flow is dominant in the melt since the dynamic Bond number is much less than the unity. The dimensionless pulling speed used by Jurisch and Löser to grow the Mo crystal is about $O(10^{-7})$, which is very small in comparison with the flow velocity in the molten zone driven by the thermocapillary force. Therefore, we

Table 1. Physical properties of Mo [3]

Properties	Mo
T_m [K]	2890
ρ_l [kg m^{-3}]	9600
ρ_s [kg m^{-3}]	9600
β [K^{-1}]	5.5×10^{-5}
ν [m^2 s^{-1}]	2.5×10^{-7}
α [m^2/s^{-1}]	1.0×10^{-5}
γ [dyn m^{-1} K^{-1}]	2.0×10^{-3}
k_s [W m^{-1} K^{-1}]	43
k_l [W m^{-1} K^{-1}]	43
c_p [J kg^{-1} K^{-1}]	436
ΔL [J kg^{-1}]	2.92×10^5

Table 2. Dimensionless parameters of Mo [3]

r_0 [mm]	Re	Gr	Bi_r	Bi_c	Bo_{dyn}
1.0	9.633×10^5	2.493×10^4	0.0050	0.0	0.03
1.3	1.252×10^6	5.476×10^4	0.0065	0.0	0.04
2.0	1.927×10^6	1.994×10^5	0.0100	0.0	0.10
3.0	2.890×10^6	6.729×10^5	0.0150	0.0	0.23

neglect the influence of the zone movement and set $V_p = 0$. The grid distribution selected by the present computation is 51×31 in the material rod, 51×81 in the molten region, and 51×31 in the crystal. For convenience, the stream function is rescaled by $\Psi = \psi \, Pr \, Re$.

Figure 2 displays the flow and temperature fields in the melt for three different values of input power P with $r_0 = 1.3$ mm. In Fig. 2, there are four toroidal cells in the molten zone. The fluid motion for the cells near the gas–melt interface, which is induced by the thermocapillary force, is much stronger than those near the zone axis, which is formed by the separation of the strong thermocapillary flow. Vigorous thermocapillary flow is confined to a very thin surface layer near the gas–melt interface. The strength of the fluid motion increases with the increase of the input power. The flow motion of the upper-half region of the molten zone is a little stronger than that of the lower-half region. Without the consideration of the buoyancy force, the flow field will be symmetric along $z = 0$. Obviously, the strength of the thermocapillary flow is assisted by the buoyancy force in the upper-half region while it is depressed in the lower-half region. The solid–liquid interface is almost symmetric along $z = 0$. It is clear that the solid–liquid interface is not mainly dominated by the buoyancy-driven flow. The four-cell flow structure was also observed by Barthel *et al.* [1], and the numerical results of the liquid-bridge model [7] also show these characteristics. The temperature field (Fig. 2) is governed by conduction because the momentum diffusion is much less than the thermal diffusion for small Prandtl fluid. The energy transport in the heated region is mainly in the radial direction. But the energy transfer in the axial direction and near the free surface enhances when the strength of thermocapillary flow increases. The thermocapillary flow becomes stronger when the magnitude of the input power increases. This is why the temperature field near the gas–melt interface is slightly distorted for higher input power. For the $NaNO_3$ material ($Pr = 9.12$), Lan and Kuo [15] always calculated two-cell flow. For higher Prandtl fluids, the influence of momentum diffusion becomes more significant than the thermal diffusion. Therefore, the energy transfer in the axial direction is strongly enhanced by the momentum transfer generated by the thermocapillary flow. As mentioned by Chen *et al.* [18], the energy transfer enhanced by the momentum transfer is used to enlarge the size of the molten zone and decreases the temperature gradients along the gas–melt interface. Therefore, the flow separation along the solid–liquid interface did not occur for $NaNO_3$ materials.

Figure 3 shows the influence of the input power on the surface temperature distribution of the molten zone for $r_0 = 1$ mm and $s = 0.775$. It is obvious that the thermocapillary convection depresses the magnitude of superheat and slightly enlarges the outer zone length. As the input power increases, the growth of the superheat is faster than that of the outer zone length. Therefore, the temperature gradient along the free surface increases with increases in the input power. The difference between the conduction and convection models increases with the increase of the input power. Figure 4 illustrates the effect of the input power on the zone lengths for two different power distributions with $r_0 = 1.3$ mm. In Fig. 4, L_s and L_c represent the zone length at the surface and the centerline of the rod. The results show that the outer zone length is greater than the inner one and the difference decreases with the increase of the magnitude of the input power. For smaller input power, the heat transport in the heated region is mainly in the radial direction, and with the increase of the input power, the growth rates of the inner and outer lengths of the molten zone increase slowly and are almost the same. For higher input power, the heat transport in the axial direction becomes significant, and, with further increase of the input power, the zone lengths grow more obvious with the inner one faster than the outer one because of the radiation lost from the surface. Because the power density of $s = 0.775$ is more condensed at the surface of the rod near $z = 0$ than it is at $s = 1.55$, the input power of $s = 0.775$ (where the growth rate of the zone length becomes significant) is much smaller than that of $s = 1.55$. For small Prandtl fluids with smaller Re, the results of Chen *et al.* [18] show that the solid–melt interface varies from convex towards the melt, through flat to concave, when the input power P increases. The present results show that the solid–melt interface is convex towards the melt to the extent of the input power P considered. With further increases of the input power, the solutions do not converge due to the stronger thermocapillary convection in the melt. From Fig. 4, we can conjecture that the present results still show this trend. The experimental observation of Jurisch and Löser [3] also showed that the steady thermocapillary flow only exists when the solid–melt interface is convex towards the melt. The maximum surface zone length, where the steady, axisymmetric thermocapillary flow can be

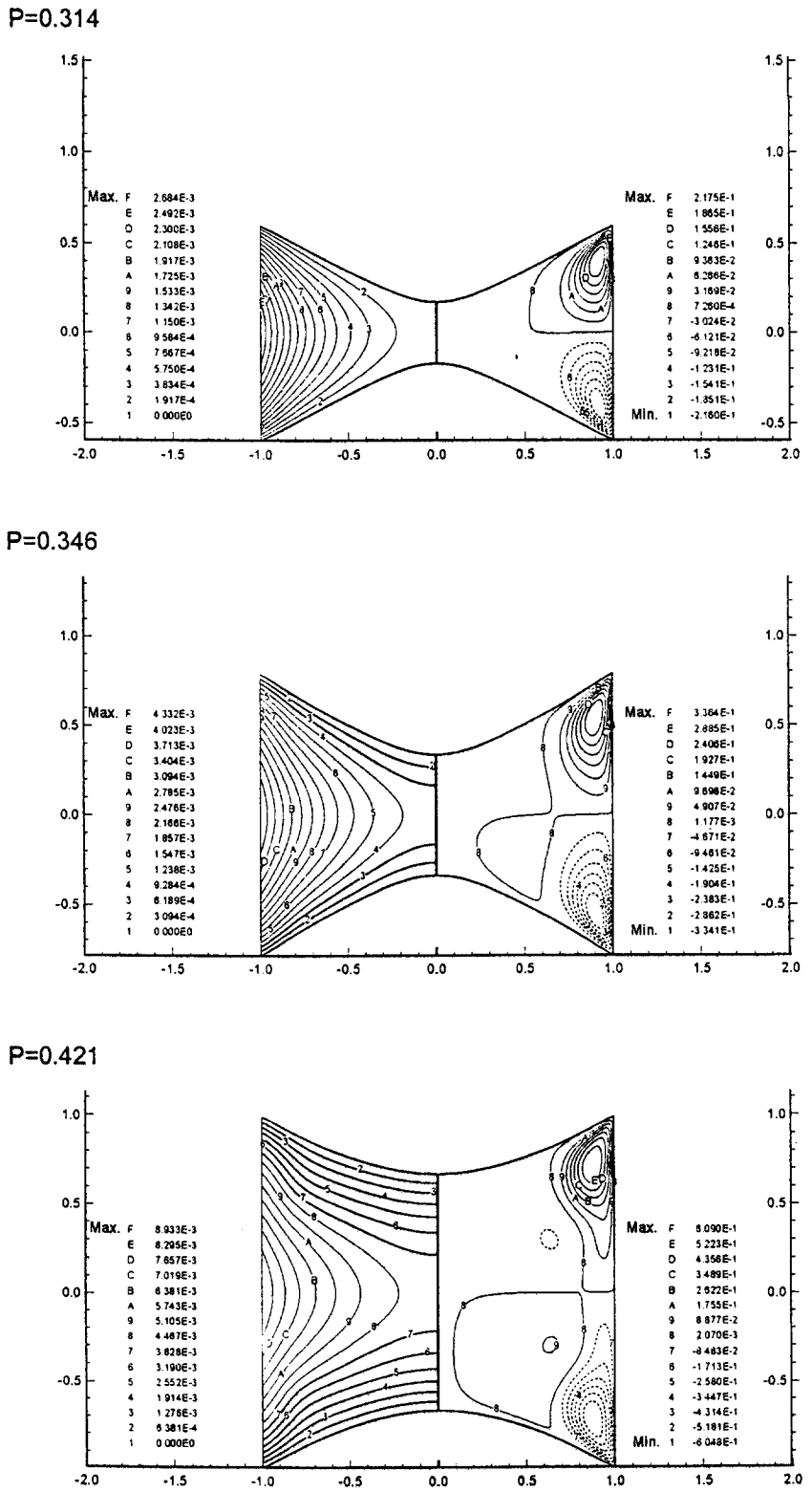

Fig. 2. Contours for streamlines and isothermals in the melt of Mo for $r_0 = 1.3$ mm and $s = 1.55$ with three different P.

obtained by the present computations, is $(L_s)_m = 2.62$ for $s = 1.55$, and $(L_s)_m = 1.79$ for $s = 0.775$.

Figure 5 shows the influence of the input power and the power distribution on the maximum temperature Θ_{max} for $r_0 = 1.3$ mm. The maximum temperature Θ_{max} also represents the temperature difference along

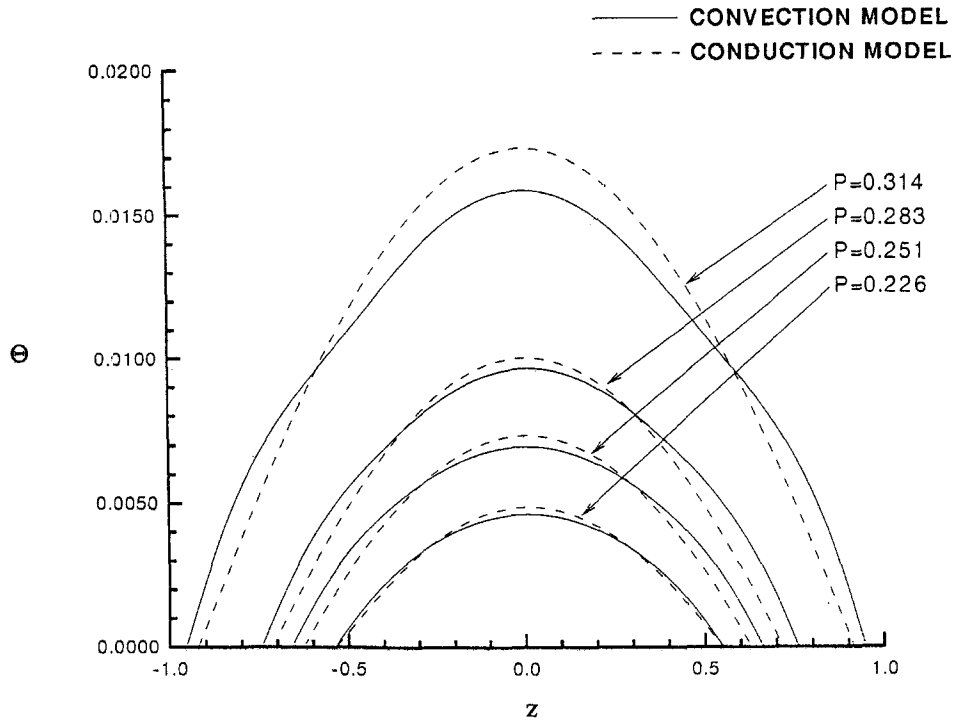

Fig. 3. Variation of the surface temperature with P for Mo with $r_0 = 1.3$ mm and $s = 0.775$. The dashed curve represents the results of the conduction model and the solid curve represents the results of the convection model.

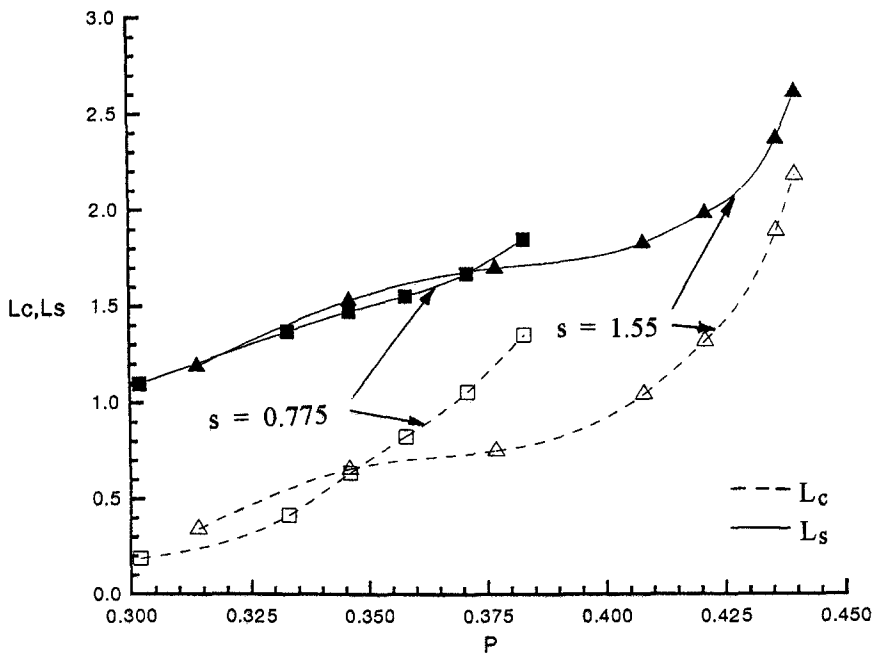

Fig. 4. Zone lengths versus input power P and power distribution for Mo with $r_0 = 1.3$ mm.

the gas–melt interface, and it increases as the input power P increases. For a fixed input power, the maximum temperature Θ_{max} for $s = 0.775$ is higher than it is for $s = 1.55$ due to the denser distribution near $z = 0$ for $s = 0.775$ (smaller heating region). Figure 6 is a plot of the maxima of the absolute value of stream function in the internal and external eddies vs P as a function of s with $r_0 = 1.3$ mm. The strength of the internal eddies is much weaker than that of the external eddies and the strength of both the internal

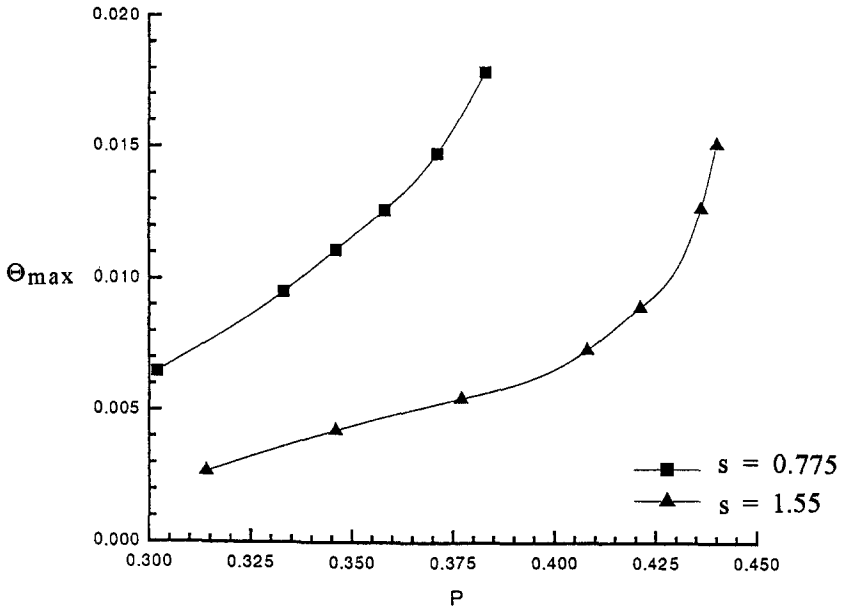

Fig. 5. Maximum temperature Θ_{max} vs input power P and power distribution for Mo with $r_0 = 1.3$ mm.

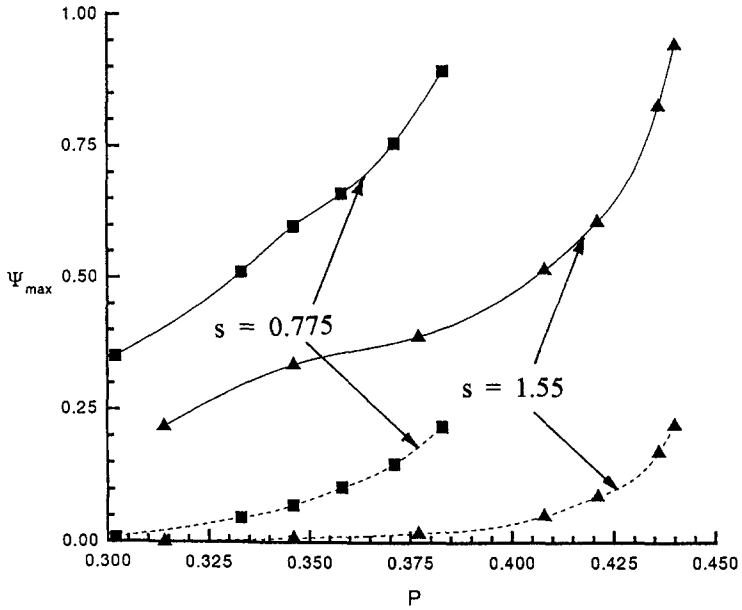

Fig. 6. Maxima of the absolute value of the stream function in the internal and external eddies versus input power P and power distribution for Mo with $r_0 = 1.3$ mm. The solid lines represent the absolute value of the stream function in the external eddies while the dashed lines designate that in the internal eddies.

and external eddies increases continuously with increasing the input power. Since convergent solutions cannot be obtained when the input power is beyond the extent considered, we conjecture from Fig. 6 that the flow instability in the melt may appear as the strength of the fluid motion reaches a certain order, which is almost independent of the input power distribution. Since the effect of the buoyancy convection is insignificant, the coordinate of the separation point in the radial direction for the upper zone is almost the same as it is for the lower zone. Figure 7 shows the variation of the radial coordinate of the separation point r_s and the radial location of the vortex center of the external eddies r_c with the input power P. From the physical viewpoint, the separation point will drift towards the melt–gas interface with the increase of the strength of thermocapillary convection and the curvature of the solid–melt interface. As the input power increases, the strength of thermocapillary flow increases (Fig. 6), and the curvature of the melt–solid

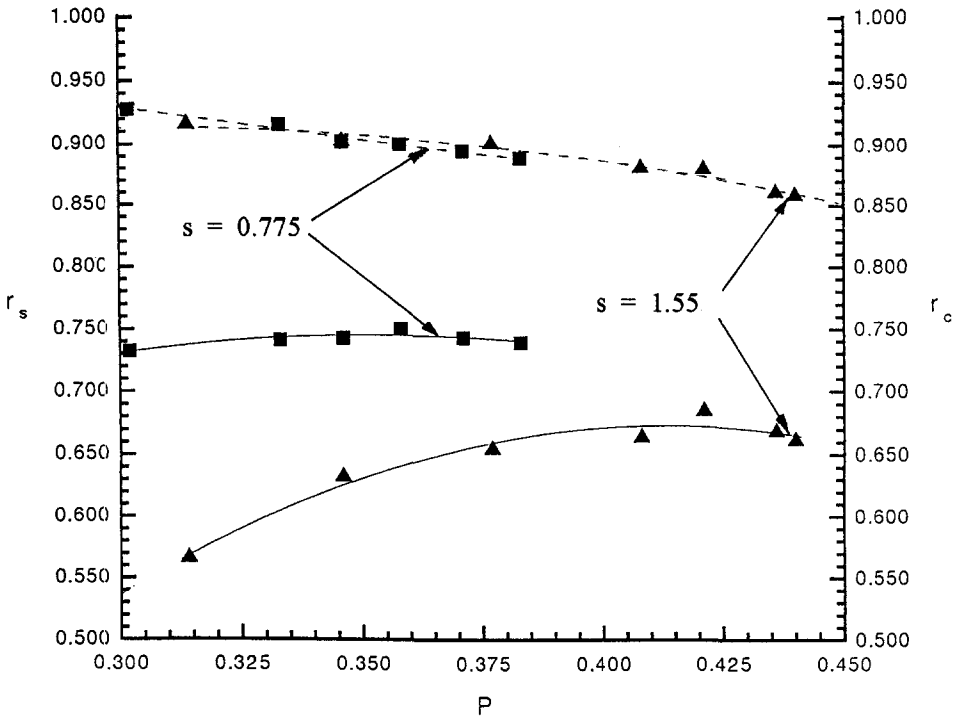

Fig. 7. Variation of the radial coordinate of the separation point r_s and the radial location of the vortex center of the external eddy r_c with input power and power distribution for Mo and $r_0 = 1.3$ mm. The solid lines denote the separation point, and the dashed lines represent the vortex center of the external eddy.

interface decreases due to the decrease of the difference between the inner and outer zone lengths (Fig. 4). With the increase of the input power, the curvature of the melt–solid interface for the higher input power changes more significantly than it does for the smaller input power. Therefore, the results of Fig. 7 show that the separation point shifts toward the melt–gas interface with the increase of the input power until the input power reaches a certain value. After this value, the separation point moves slowly toward the core region. The separation point for $s = 0.775$ is closer to the gas–liquid interface than it is for $s = 1.55$. The radial position of the vortex center of the external eddies is slightly affected by the magnitude of the input power and it is almost independent of the heating distribution. It continuously drifted away from the liquid–gas interface with the increase in input power.

The experiments of the liquid-bridge model usually use the dimensionless Marangoni number, $Ma = Pr\,Re\,\Theta_{max}L_s/2$, to characterize the flow structure of thermocapillary convection. Figure 8 shows the variation of the Marangoni number, Ma, with the surface zone length L_s. The solid lines represent the results calculated by the convection model, while the dash lines are those obtained by the conduction model. The Marangoni number increases as the outer zone length increases. Obviously, the Marangoni numbers calculated by the conduction model are higher than those obtained by the convection model. The discrepancy increases with the increases of the outer zone length. The maximum magnitude of the Marangoni number Ma_m, where the solutions of steady, axisymmetric thermocapillary flow can be obtained by the present computations, is about 602 for $s = 1.55$ and 504 for $s = 0.775$.

The effect on the rod diameter are displayed in Figs. 9–12. From Table 2, we can see that the radiation Biot number increases with the increase of the rod diameter. It means that the radiation heat loss to the surrounding increases as the diameter of the rod increases. This is why in Fig. 9 the power requirement to form a molten zone increases with the increase of the rod diameter when the power distribution is fixed at $s = 1.55$. The trends of the variations in the zone lengths with the input power for the different rod diameters are similar. As the radiation Biot number increases, the growth rate of the inner and outer zone lengths (with the increase of the input power) decreases and the difference between the inner and outer zone lengths increase. It means that the curvature of the melt–solid interface increases with the increase of the Biot number. From Table 3, it is clear that the maximum dimensionless outer zone length $(L_s)_m$ decreases when the rod diameter r_0 increases. The results show similar trends with the rod diameter as the critical outer zone length at the transition from a steady, axisymmetric thermocapillary flow to an oscillatory flow as measured by Jurisch and Löser [3]. In Fig. 10, the convergent solution of an axisymmetric, steady flow cannot be obtained above the extent of the power considered. We can conjecture that the instability is a strong function of the strength of ther-

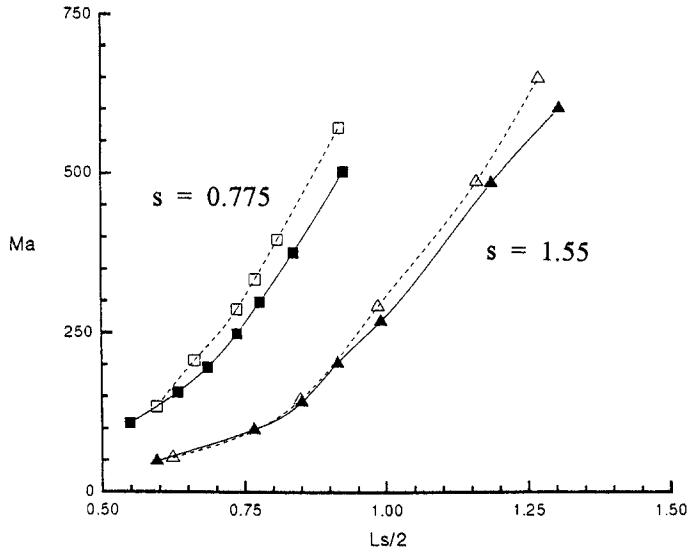

Fig. 8. Marangoni number Ma vs surface zone length L_s and power distribution for Mo and $r_0 = 1.3$ mm. The dashed lines represent the results based on the conduction model, and the solid lines designate the results of the convection model.

Table 3. Results for Mo with $s = 1.55$

r_0 [mm]	$(L_s)_m$	Ma_m	$(L_s)_c$†	Ma_c†
1.3	2.6	602	2.6	638
2.0	2.3	818	2.2	925
3.0	1.8	794	1.8	1625

† These results were obtained by Jurisch and Löser [3].

mocapillary flow and is almost independent of the magnitude of the rod diameter. In Fig. 11, the results show that the trends of the variation of r_c and r_s with P for the different rod diameters are similar. The vortex center does not change significantly with the variation of the rod diameter, and the separation point moves towards the gas–melt interface with the increase of the rod diameter. Figure 12 shows that

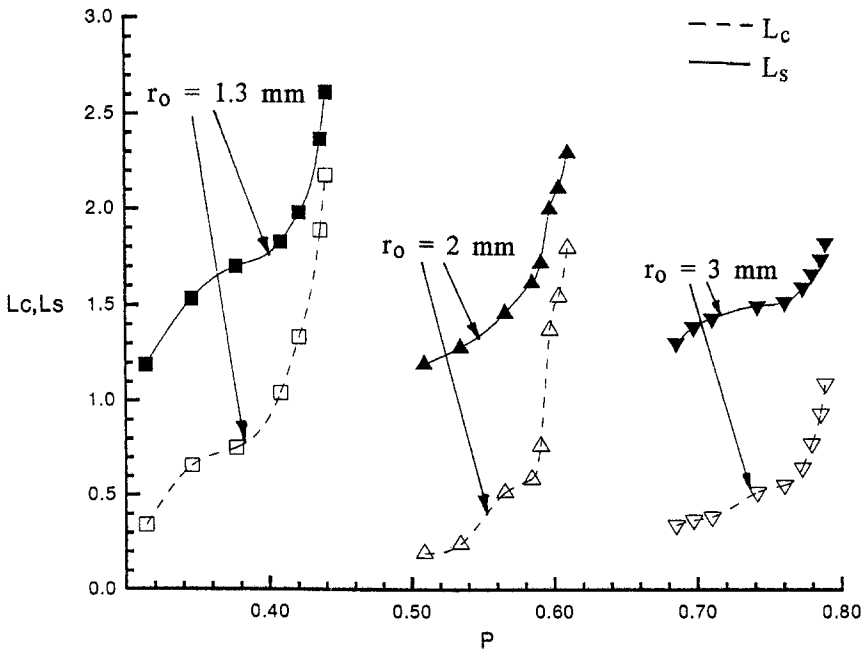

Fig. 9. Zone lengths vs input power P and rod radius r_0 for Mo with $s = 1.55$.

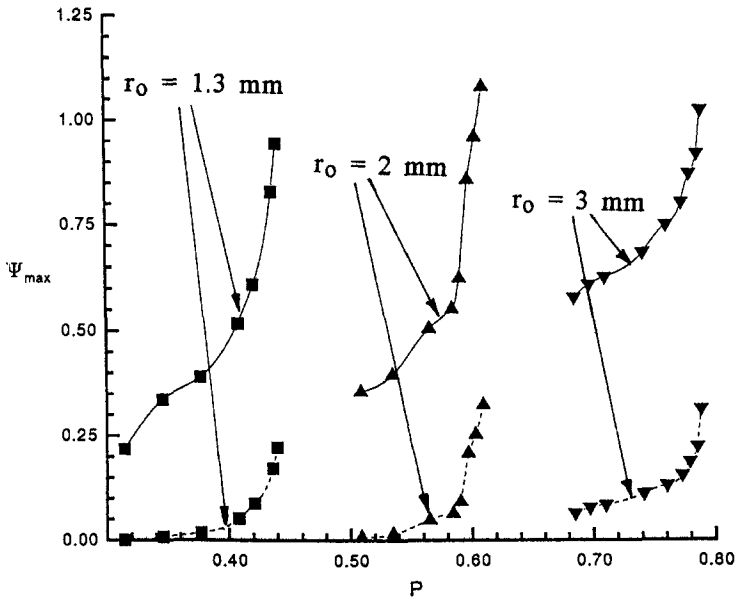

Fig. 10. Maxima of the absolute value of the stream function in the internal and external eddies versus input power P and rod radius r_0 for Mo with $s = 1.55$. The solid lines represent the absolute value of the stream function in the external eddies, while the dashed lines designate that in the internal eddies.

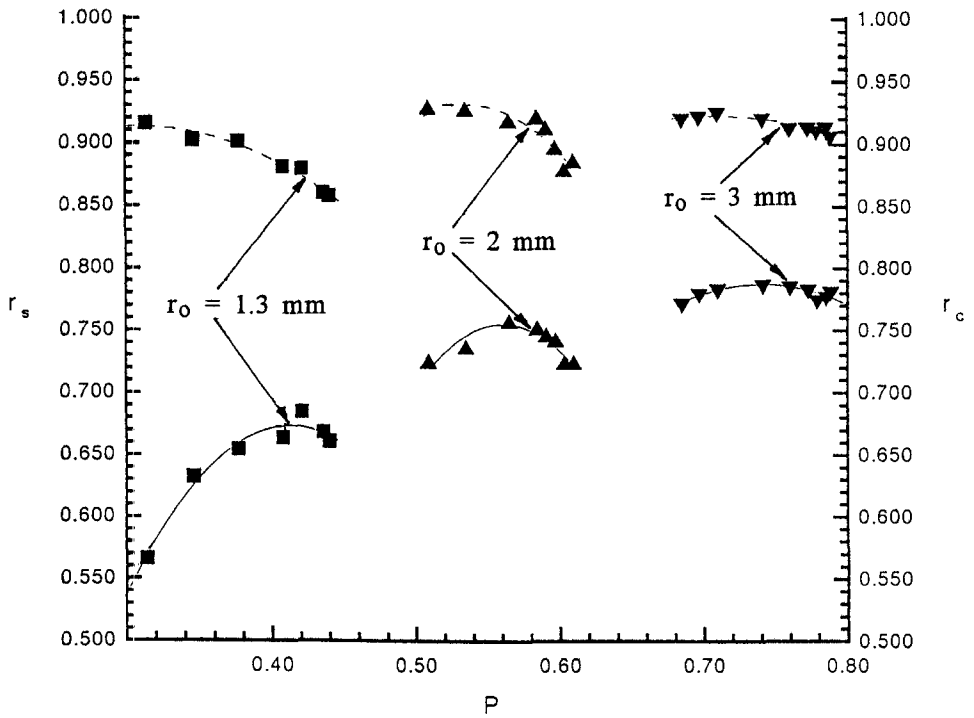

Fig. 11. Variation of the radial coordinate of the separation point r_s and the radial location of the vortex center of the external eddies r_c with input power and rod radius r_0 for Mo with $s = 1.55$. The solid lines denote the separation point, and the dashed lines represent the vortex center of the external eddy.

for a fixed outer zone length the Marangoni number increases with the increases of the rod diameter. The growth rate of the Marangoni number with the increase of the outer zone length increases as the rod diameter increases. Jurisch and Löser [3] estimated the critical Marangoni number based on the critical zone length measured from the interior structure of the resultant crystals and the surface temperature difference calculated from the numerical solution of the conduction model. The power distribution for

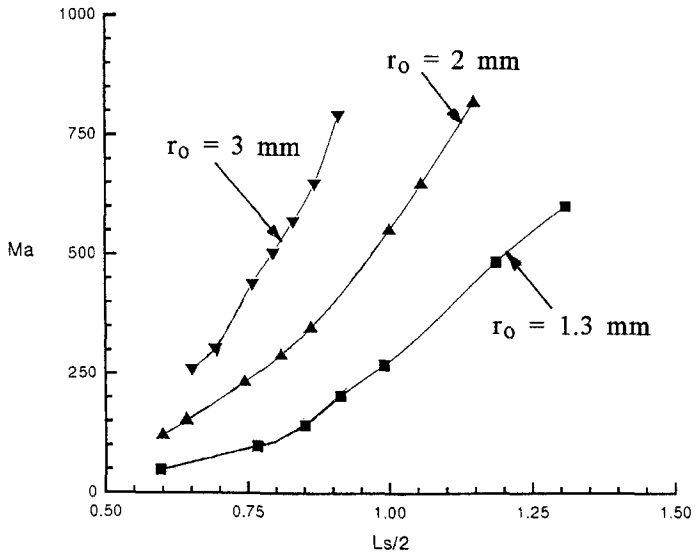

Fig. 12. Marangoni number Ma vs surface zone length L_s and radius r_0 for Mo with $s = 1.55$.

$s = 1.55$ is similar to that used by Jurisch and Löser to melt the material rod with $r_0 = 1.3$ and 2 mm. From Fig. 8, we can conclude that the critical Marangoni number is overpredicted by using the conduction analysis. If the critical Marangoni number predicted by Jurisch and Löser is corrected by using the temperature difference calculated from the convection model, the maximum magnitude of the Marangoni numbers for $r_0 = 1.3$ and 2 mm obtained by the present computations are very close to the critical Marangoni number predicted by them. For $r_0 = 3$ mm, the critical Marangoni number is much higher than the present results. From Fig. 12, we can expect that for $L_s/2 \approx 1.8$ the Marangoni number will increase sharply as the outer zone length increases slightly. The difference for $r_0 = 3$ mm may be caused by the several factors. One is the error generated by the discrepancy between the power distribution assumed by the present computation and that used by Jurisch and Löser. Other possibilities are due to the conduction model and the uncertainty of the experiments.

5. CONCLUSIONS

Computations have been performed to investigate the flow structure in the floating zone crystal-growth process for molybdenum materials. The thermocapillary convection is dominant for the rod diameter considered in the present study. The present results are consistent with those observed by Barthel *et al.* [1] in that four toroidal cells always appear in the melt. The convergent solution for a steady, axisymmetric flow can not be obtained when the strength of the flow reaches a certain order, which varies insignificantly with the change of the heating region and the rod diameter. Beyond this value, we conjecture that an oscillatory flow may appear. The maximum outer zone length obtained by the present computation decreases with the increase of the rod diameter and the decrease of the heating region. They are in qualitative and quantitative agreement with the critical outer zone length measured by Jurisch and Löser [3]. The theoretical prediction of the critical surface zone length can be obtained using a stability analysis. The linear stability analysis using the flow and temperature states obtained by the present computation has been performed by Chin [21]. The critical surface zone length predicted by the linear theory is slightly less than the maximum surface zone length calculated by the present computation.

The maximum Marangoni number calculated by the present computations is less than the critical Marangoni number obtained by Jurisch and Löser [3]. From our results, it is clear that the critical Marangoni numbers of Jurich and Löser are overestimated since the surface temperature difference is calculated using a conduction model. We believe that a better agreement may be obtained if the power distribution selected by us is closer to that used by Jurich and Löser, and the results of Jurich and Löser are corrected using the surface temperature calculated from the convection model.

The magnitudes of the Reynolds and Grashof number for silicon materials are about $O(10^6)$ and $O(10^3)$, respectively. Therefore, we can expect that the silicon materials will show physical behaviors similar to the predictions for the molybdenum materials as predicted by the present computations.

Acknowledgement—The authors gratefully acknowledge the support of the National Science Council of the R.O.C. for this work through grant No. NSC83-0401-E008-032.

REFERENCES

1. J. Barthel, K. Eichler, M. Jurisch, and W. Löser, On the significance of surface tension driven flow in floating-zone melting experiments, *Kristall Technik* **14,** 637–644 (1979).
2. A. Eyer, H. Leiste and R. Nitsche, Floating zone growth of silicon under microgravity in a sounding rocket, *J. Crystal Growth* **71,** 173–182 (1985).
3. M. Jurisch and W. Löser, Analysis of periodic non-rotational W striations in Mo single crystals due to non-steady thermocapillary convection, *J. Crystal Growth* **102,** 214–222 (1980).
4. K. Kitamura, S. Kimura and S. Hosoya, The interface shapes of some oxide materials grown by the floating zone method, *J. Crystal Growth* **48,** 469–472 (1980).
5. C. E. Chang and W. R. Wilcox, Analysis of surface tension driven flow in floating zone melting, *Int. J. Heat Mass Transfer* **19,** 335–366 (1976).
6. N. Kobayashi, Computer simulation of the steady flow in a cylindrical floating zone under low gravity, *J. Crystal Growth* **66,** 63–72 (1984).
7. M. Jurisch, W. Löser, E. Lyumkis, E. Martuzane and B. Martuzans, Connection of the thermocapillary flow characteristics and the impurity distribution pattern in floating zone molten molybdenum single crystals, *Crystal Res. Technol.* **17,** 963–971 (1982).
8. B. Fu and S. Ostrach, Numerical solution of thermocapillary flows in floating zones. In *Transport Phenomena in Materials Processing*. ASME, New York (1985).
9. J.-C. Chen, J.-C Sheu and Y.-T. Lee, Maximum stable length of nonisothermal liquid bridges, *Phys. Fluids A* **2,** 1118–1123 (1990).
10. D. Schwabe, A. Scharmann, F. Preisser and R. Oeder, Experiments on surface tension driven flow in floating zone melting, *J. Crystal Growth* **43,** 305–312 (1978).
11. C.-H. Chun, Experiments on steady and oscillatory temperature distribution in a floating zone due to the Marangoni convection, *Acta Astronautica* **7,** 479–488 (1980).
12. Y. Kamotani, S. Ostrach and M. Vargas, Oscillatory thermocapillary convection in a simulated floating-zone configuration, *J. Crystal Growth* **66,** 83–90 (1984).
13. F. Preisser, D. Schwabe and A. Scharmann, Steady and oscillatory thermocapillary convection in liquid columns with free cylindrical surface, *J. Fluid Mech.* **126,** 545–567 (1983).
14. R. Velten, D. Schwabe and A. Scharmann, The periodic instability of thermocapillary convection in cylindrical liquid bridges, *Phys. Fluids A* **3,** 267–279 (1991).
15. C. W. Lan and S. Kuo, Thermocapillary flow and melt–solid interfaces in floating-zone crystal growth under microgravity, *J. Crystal Growth* **102,** 1043–1058 (1990).
16. C. W. Lan and S. Kuo, Heat transfer, fluid flow and interface shapes in floating-zone crystal growth, *J. Crystal Growth* **108,** 351–366 (1991).
17. C. W. Lan and S. Kuo, Effects of rotation on heat transfer, fluid flow and interfaces in normal gravity floating-zone crystal growth, *J. Crystal Growth* **114,** 517–535 (1991).
18. J.-C. Chen, C.-F. Chu and W.-F. Ueng, Thermocapillary convection and melt–solid interface in the floating zone, *Int. J. Heat Mass Transfer* **37,** 1733–1748 (1994).
19. J. F. Thompson, F. C. Thames and W. Mastin, Automatic numerical generation of body fitted curvilinear coordinate system for field containing any number of arbitrary two-dimensional bodies, *J. Comput. Phys.* **15,** 299–319 (1974).
20. J. F. Middlecoff and P. D. Thomas, Direct control of the grid point distribution in meshes generated by elliptic equations, *AIAA J.* **18,** 652–656 (1980).
21. G.-H. Chin, Linear stability analysis of thermocapillary convection in the floating zone, Master Thesis, National Central University, Chung-Li, Taiwan (1994).